

# *In planta* study of photosynthesis and photorespiration using NADPH and NADH/NAD<sup>+</sup> fluorescent protein sensors

Shey-Li Lim <sup>1</sup>, Chia Pao Voon <sup>1</sup>, Xiaoqian Guan <sup>1</sup>, Yi Yang <sup>2</sup>, Per Gardeström <sup>3</sup> & Boon Leong Lim <sup>1,4,5</sup>✉

The challenge of monitoring *in planta* dynamic changes of NADP(H) and NAD(H) redox states at the subcellular level is considered a major obstacle in plant bioenergetics studies. Here, we introduced two circularly permuted yellow fluorescent protein sensors, iNAP and SoNar, into *Arabidopsis thaliana* to monitor the dynamic changes in NADPH and the NADH/NAD<sup>+</sup> ratio. In the light, photosynthesis and photorespiration are linked to the redox states of NAD(P)H and NAD(P) pools in several subcellular compartments connected by the malate-OAA shuttles. We show that the photosynthetic increases in stromal NADPH and NADH/NAD<sup>+</sup> ratio, but not ATP, disappear when glycine decarboxylation is inhibited. These observations highlight the complex interplay between chloroplasts and mitochondria during photosynthesis and support the suggestions that, under normal conditions, photorespiration supplies a large amount of NADH to mitochondria, exceeding its NADH-dissipating capacity, and the surplus NADH is exported from the mitochondria to the cytosol through the malate-OAA shuttle.

<sup>1</sup>School of Biological Sciences, University of Hong Kong, Pokfulam, Hong Kong, China. <sup>2</sup>Synthetic Biology and Biotechnology Laboratory, State Key Laboratory of Bioreactor Engineering, Shanghai Collaborative Innovation Center for Biomanufacturing Technology, East China University of Science and Technology, Shanghai, China. <sup>3</sup>Umeå Plant Science Centre, Department of Plant Physiology, Umeå University, SE-901 87 Umeå, Sweden. <sup>4</sup>State Key Laboratory of Agrobiotechnology, The Chinese University of Hong Kong, Hong Kong, China. <sup>5</sup>HKU Shenzhen Institute of Research and Innovation, Shenzhen, China. ✉email: [blim@hku.hk](mailto:blim@hku.hk)

Adenosine triphosphate (ATP), nicotinamide adenine dinucleotide phosphate (NADPH), and nicotinamide adenine dinucleotide (NADH) are crucial energy molecules in living systems. Numerous studies have measured these metabolites *in vitro*, using bioluminescence, HPLC, mass spectrometry, enzymatic, and radioactive methods. However, *in vitro* methods require the extraction of ATP, NADPH, and NADH from tissues before measurements can be carried out<sup>1</sup> and therefore cannot determine the instant levels of these metabolites in different subcellular compartments of different cells in a tissue.

Recently, our group has employed a novel MgATP<sup>2-</sup>-specific Förster resonance energy transfer (FRET)-based sensor to study the *in vivo* ATP levels of the plastids and cytosol of different tissues in *Arabidopsis thaliana* (*Arabidopsis*)<sup>2</sup>. A change in the FRET signal reflects a change in MgATP<sup>2-</sup> concentration. By using this ATP sensor and a pH sensor, we have shown that the stromal ATP concentration is significantly lower than the cytosolic ATP concentration; that the import of ATP into mature chloroplasts is impeded by the downregulation of nucleotide transporters; that cytosolic ATP does not enter mature chloroplasts and is, therefore, unlikely to support the Calvin–Benson–Bassham (CBB) cycle; that, instead of ATP import, in *Arabidopsis* it is the export of reducing equivalents from chloroplasts that balances the NADPH/ATP supply from the linear electron flow and the NADPH/ATP demand of the CBB cycle<sup>2</sup>. Here, we employed two circularly permuted yellow fluorescent protein-based protein sensors, iNAP<sup>3</sup> and SoNar<sup>4</sup>, to measure the *in planta* dynamic changes of NADPH and the NADH/NAD<sup>+</sup> ratio induced by illumination in several subcellular compartments of *Arabidopsis* plants. These sensors were engineered from the bacterial Rex repressor capable of sensing pyridine dinucleotides redox states, and have many desirable properties such as intense fluorescence, rapid response, high specificity, and large dynamic range. Similar to the FRET based ATP sensor, the measurements of these sensors are also ratio-metric and are less prone to the varied sensor expression levels in different tissues and compartments. We used stably transformed lines expressing these sensors to investigate photosynthesis and photorespiration.

Ribulose-1,5-bisphosphate carboxylase/oxygenase (Rubisco) carries out the initial step in the fixation of CO<sub>2</sub> during photosynthesis. Rubisco is a slow enzyme, with a  $k_{\text{cat}}$  of 1–10 s<sup>-1</sup><sup>5</sup>. Although it has a selectivity for CO<sub>2</sub> over O<sub>2</sub> of almost a factor of 100, due to the much higher concentration of O<sub>2</sub> (21%) than CO<sub>2</sub> (0.4%) in the atmosphere, it is estimated that for every three CO<sub>2</sub> molecules fixed in C3 plants, about one O<sub>2</sub> molecule is mistakenly utilized by Rubisco to generate one 3-phosphoglycerate (3-PG) and one 2-phosphoglycolate (2-PG) molecule<sup>6,7</sup>. The recycling of the photorespiration product 2-PG back to 3-PG involves eight enzymatic steps in chloroplasts, mitochondria, and peroxisomes. Hence, photorespiration has been regarded as a wasteful process due to the additional consumption of stromal ATP and liberation of CO<sub>2</sub> in mitochondria in the cycle<sup>8</sup>.

During photorespiration, one NADH, one CO<sub>2</sub>, and one NH<sub>3</sub> molecule are generated in the mitochondria through the conversion of two glycine molecules to one serine cooperatively by glycine decarboxylase (GDC) and serine hydroxymethyl transferase (SHMT). A certain amount of serine is exported to the cytosol for other uses<sup>9</sup>, whereas most is imported into peroxisomes and converted into hydroxypyruvate, which is then reduced to glycerate by hydroxypyruvate reductase (HPR), at the expense of NADH molecules. By converting the malate imported into the organelle, peroxisomal NAD-dependent malate dehydrogenase (NAD-MDH) provides the NADH required for hydroxypyruvate reduction<sup>10</sup>.

During photosynthesis, the linear electron flow (LEF) generates ATP and NADPH at a ratio of 1.28<sup>11</sup>, whereas the CBB cycle requires ATP and NADPH at a 1.5 ratio, resulting in a deficiency of ATP<sup>12</sup> or an excess of NADPH<sup>13</sup>. Although the cyclic electron flow can contribute extra ATP, mature mesophyll chloroplasts are unable to import cytosolic ATP<sup>2</sup>. Hence, chloroplasts must recycle excess NADPH into NADP<sup>+</sup> to serve as the electron acceptor during photosynthesis to balance the ratio of stromal ATP to NADPH.

In chloroplasts, NADP<sup>+</sup> is recycled from NADPH via three major routes: the CBB pathway and 3-phosphoglyceric acid/triose phosphate (PGA/TP) exchange coupled with it, fatty acid synthesis, and the malate-oxaloacetate (malate-OAA) shuttle. Excess NADPH generated from the LEF can be exported to the cytosol through the shuttle in the form of malate via the action of NADP-dependent malate dehydrogenase (NADP-MDH)<sup>14,15</sup>, which converts OAA into malate and regenerates NADP<sup>+</sup><sup>16</sup>. Hence, during daytime, malate builds up in leaf cells, where most of it is stored in the vacuole, whereas the cytosolic malate concentration is maintained at a relatively constant, low level<sup>17</sup>. Some cytosolic malate is imported into the peroxisomes, where it is used by peroxisomal NAD-MDH to recycle OAA and regenerate the NADH required for hydroxypyruvate reduction<sup>10</sup>. In mitochondria, both the malate-OAA shuttle<sup>12,16,18–22</sup> and photorespiration<sup>23,24</sup> have been proposed to provide reducing equivalents to the mitochondrial electron transport chain (mETC) for ATP production. In a flux balance model of the mature leaves of C3 plants, both photorespiration and the malate-OAA shuttle are predicted to contribute to feeding NADH into the mETC<sup>25</sup>. Experimental data obtained from barley leaf protoplasts<sup>23,24,26</sup> and isolated mitochondria<sup>27</sup> suggest that photorespiration is the major source of reducing equivalents to the mETC. However, this has not been examined in a whole plant level, and the direction of the flow of reducing equivalents between different subcellular compartments during photosynthesis has not yet been fully resolved<sup>28</sup>.

Here, by employing a NADPH and a NADH/NAD<sup>+</sup> sensors, we examined *in planta* dynamic changes in the NADPH pools and NADH/NAD<sup>+</sup> ratio in the stroma and cytosol upon illumination. We suggest that, at the light intensities we used, photorespiration supplies a large amount of reducing equivalents to mitochondria during photosynthesis, which exceeds the NADH-dissipating capacity of the mETC. Consequently, the surplus NADH must be exported from the mitochondria to the cytosol through the mitochondrial malate-OAA shuttle.

## Results

**Establishing iNAP and SoNar sensors in *Arabidopsis*.** We generated multiple transgenic *Arabidopsis* lines in the wild-type (WT, Col-0) background expressing a high-affinity NADPH sensor (iNAP1), a low-affinity NADPH sensor (iNAP4), and an NADH/NAD<sup>+</sup> sensor (SoNar) in the cytosol (Supplementary Fig. 1). These cytosolic sensors were occasionally seen in the nucleus in some tissues (e.g. guard cells). We also fused the iNAP1, iNAP4, and SoNar sensors with organelle-specific targeting peptides to direct their expression specifically to the plastid stroma and peroxisome. In addition, we generated *Arabidopsis* lines expressing iNAPc (Supplementary Fig. 1f–h), in which the ligand binding to pyridine nucleotides is fully abolished in each of these compartments, to serve as a pH control<sup>3</sup>. At least two independent lines expressing each sensor in each compartment were selected for analysis. No abnormal phenotype was observed for these lines, and the plant size did not show significant differences among lines (Supplementary Fig. 1i, j). We imaged the seedlings using a confocal microscope configured to detect

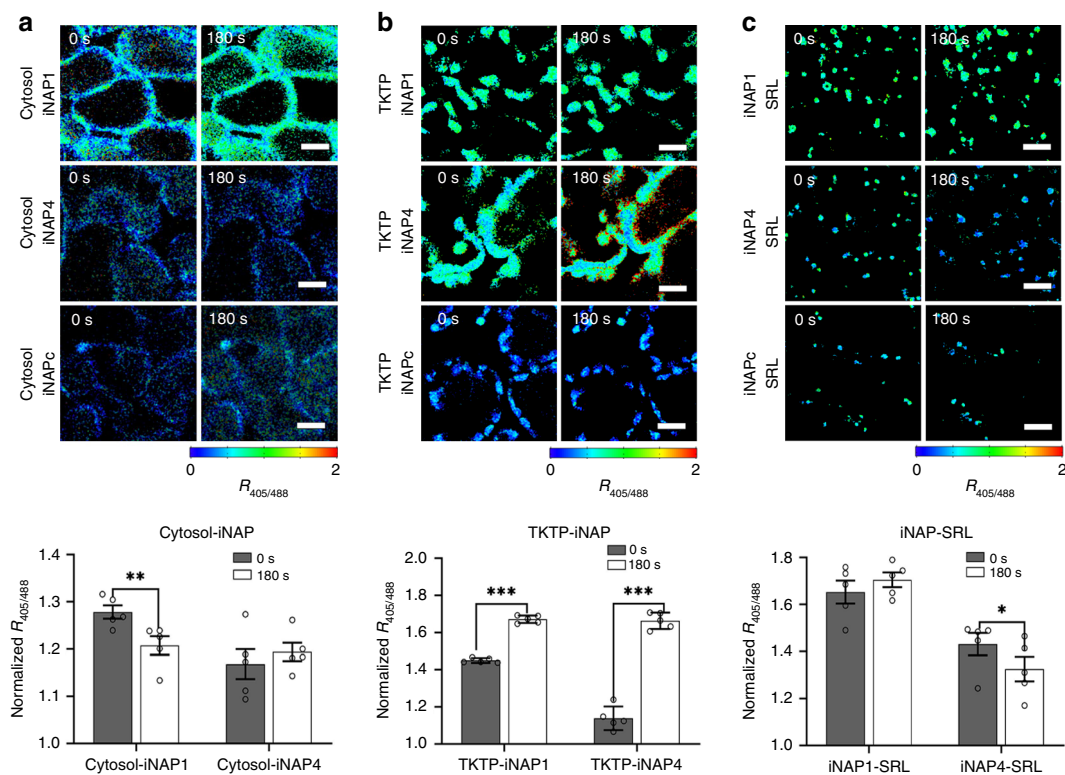


**Fig. 1** Light responses of iNAP sensors in different compartments of 10-day-old cotyledon mesophyll. **a** Seedlings expressing cytosolic iNAP1, iNAP4, and iNAPc. **b** Seedlings expressing stromal iNAP1, iNAP4, and iNAPc, and **c** seedlings expressing peroxisomal iNAP1, iNAP4, and iNAPc were continuously illuminated for 180 s at  $296 \mu\text{mol m}^{-2} \text{s}^{-1}$  ( $n = 5$ ; error bars  $\pm$  SEM). Emissions at 520 nm after sequential excitation at 405 nm and 488 nm were recorded, and the ratios of the two emissions ( $R_{405/488}$ ) are presented in pseudocolor image, where high ratios (red) correspond to high NADPH levels. Scale bars, 20  $\mu\text{m}$ . Asterisks indicate statistical significance as determined using paired  $t$ -test: \* $P < 0.05$ , \*\* $P < 0.01$ , \*\*\* $P < 0.001$ .

chlorophyll autofluorescence (excitation at 488 nm and emission at 629–700 nm). The presence of iNAP and SoNar fluorescence in the peripheral cytoplasm indicated that these sensors were expressed in the cytosol (Supplementary Fig. 2a), whereas the fluorescence signals of TKTP-iNAP and TKTP-SoNar (fusions of the plastid-specific chloroplast transketolase transit peptide, TKTP, from *Nicotiana tabacum*) co-localized with chlorophyll autofluorescence, corroborating the chloroplast expression of both sensors (Supplementary Fig. 2b). We also compared the distribution of iNAP4-SRL and iNAPc-SRL (fusions of iNAP4 and iNAPc with the peroxisome marker peroxisomal targeting signal type 1, SRL) with that of mRFP-SRL (a fusion of red fluorescent protein with SRL) using transient protoplast transformation. Both iNAP4-SRL and iNAPc-SRL co-localized with mRFP-SRL in a typical peroxisome pattern visualized in spherical spots, suggesting that both sensors were targeted specifically to peroxisomes (Supplementary Fig. 2c). However, no Arabidopsis lines expressing SoNar-SRL were obtained after repeated transformation attempts. We also failed to introduce these sensors into mitochondria of WT and *suppressor of gene silencing 3-13* (*sgs3-13*)<sup>29</sup> lines using the presequence that successfully targeted GFP and the pH sensor cpYFP to mitochondrial matrix (Supplementary Fig. 2d)<sup>30,31</sup>.

**NADPH levels are lower in cytosol than in plastid stroma and peroxisome.** To identify the iNAP sensors with the most suitable affinity for each compartment, we introduced iNAP sensors with high (iNAP1) and low (iNAP4) NADPH affinities into the cytosol, plastid stroma, and peroxisome. Since the iNAP1 and iNAP4 sensors are highly specific to NADPH<sup>3</sup>, and NADPH is

produced during photosynthesis, the response of these sensors can be studied by illuminating the plants. Illumination at  $296 \mu\text{mol m}^{-2} \text{s}^{-1}$  did not significantly affect the cytosolic iNAP4 ratio (Fig. 1a), but it decreased the cytosolic iNAP1 ratio significantly ( $P < 0.01$ ), suggesting that the cytosolic NADPH pool was diminished upon exposure to light. Illumination caused significant ( $P < 0.001$ ) ratiometric shifts for both the TKTP-iNAP4 and TKTP-iNAP1 sensors (Fig. 1b). However, TKTP-iNAP4 exhibited a greater ratio increment, suggesting that the iNAP1 signal was saturated upon illumination; we therefore used TKTP-iNAP4 throughout the remainder of our study.

In peroxisomes, illumination caused a significant decrease ( $P < 0.05$ ) in the ratio of the low-affinity iNAP4-SRL sensor lines but not the high-affinity iNAP1-SRL lines (Fig. 1c), indicating that the NADPH concentration in peroxisomes exceeded the maximum dynamic limit of the iNAP1 sensor. Similar responses were not observed in illuminated roots, suggesting that the responses observed in the mesophyll were due to photosynthesis (Fig. 2). Together, the differences in saturation response between iNAP1 and iNAP4 in these compartments suggest that the NADPH level in the cytosol is lower than those in plastid stroma and peroxisome in Arabidopsis. For further *in planta* analyses, we employed cytosolic iNAP1, TKTP-iNAP4, and iNAP4-SRL Arabidopsis lines.

To test the *in vitro* and semi *in vivo* characteristics of the sensor proteins, we adopted recombinant proteins and seedling root tips to monitor the specificity of NADPH and NADH/NAD<sup>+</sup> binding affinity curves. The *in vitro*  $K_d$  values determined for iNAP1 and iNAP4 at 22 °C were 0.3  $\mu\text{M}$  and 30  $\mu\text{M}$ , respectively, which were much lower than the values 2.0  $\mu\text{M}$  and 120  $\mu\text{M}$  obtained at 37 °C<sup>3</sup>. The  $K_{\text{NADH/NAD}^+}$  of SoNar at 22 °C was determined to be

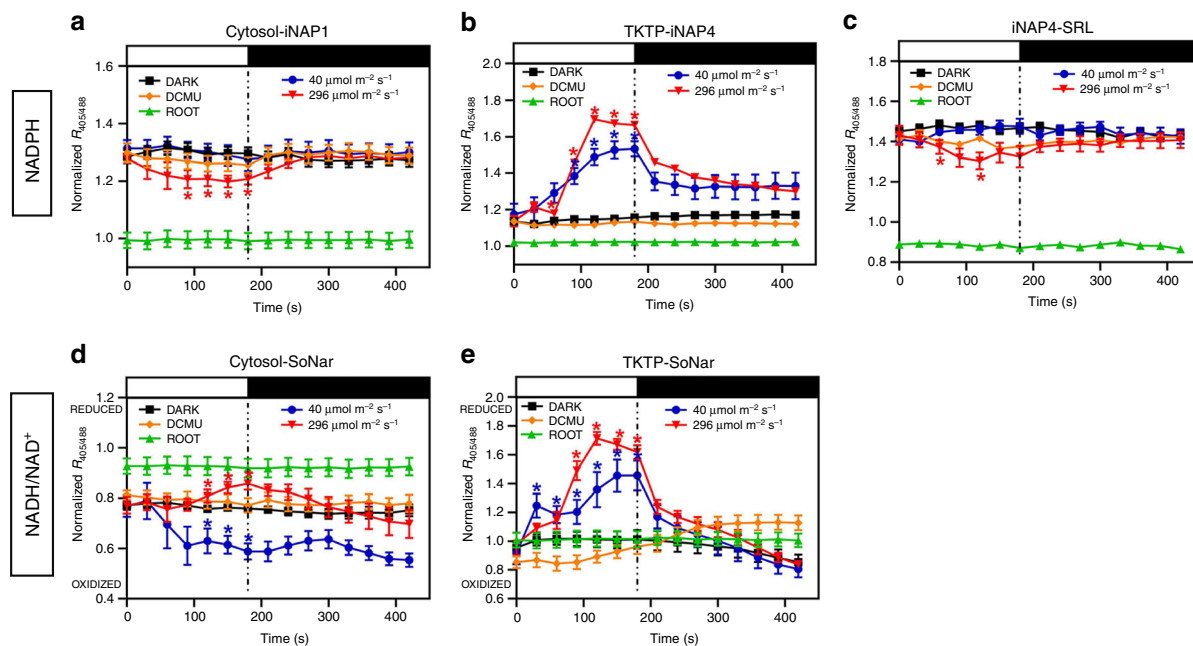


**Fig. 2** Light responses of iNAP and SoNar sensors in untreated cotyledon with  $40 \mu\text{mol m}^{-2} \text{s}^{-1}$  or  $296 \mu\text{mol m}^{-2} \text{s}^{-1}$  illumination or cotyledon pre-treated with DCMU or root at  $296 \mu\text{mol m}^{-2} \text{s}^{-1}$  illumination. The normalized  $R_{405/488}$  shifts of **a** cytosolic iNAP1, **b** stromal iNAP4, **c** peroxisomal iNAP4, **d** cytosolic SoNar, and **e** stromal SoNar in mesophyll of 10-day-old cotyledon in response to illumination with an interval of 30 s are shown. Illumination up to 180 s is represented by white bars, and the period after light was turned off is indicated by black bars ( $n = 5$ ; error bars  $\pm$  SEM). All results shown were normalized with cytosol-iNAPc, TKTP-iNAPc, and iNAPc-SRL, respectively. Asterisks indicate that the differences ( $P < 0.05$ ) between results from the dark condition and  $40 \mu\text{mol m}^{-2} \text{s}^{-1}$  or  $296 \mu\text{mol m}^{-2} \text{s}^{-1}$  illumination are statistically significant as determined by a paired *t*-test. DCMU, 3-(3,4-dichlorophenyl)-1,1-dimethylurea.

0.04 (Supplementary Fig. 3), which was slightly higher than the value (0.025) obtained at  $37^\circ\text{C}$ <sup>32</sup>. In semi *in vivo* conditions, the sensors displayed increasing ratios at a higher level or ratio of exogenous nucleotides (Supplementary Fig. 4), where the  $K_d$  values for iNAP1, iNAP4, and  $K_{\text{NADH/NAD}^+}$  for SoNar were calculated as 2.5, 5.6, and  $1.48 \mu\text{M}$ , respectively, which were different from the values obtained *in vitro*. However, the values determined by the semi *in vivo* protocol might be affected by possible artifacts. First, there are endogenous NADPH in the root cells and zero value could not be set. As a result, the  $K_d$  value for iNAP1 would be overestimated. Second, the ratios of many cells in the root tips were averaged for ratio calculation but the degree of penetration of exogenous NADPH into different cells varied. This could lead to an underestimation of the  $K_d$  value for iNAP4. Nonetheless, the semi *in vivo* experiments showed that the sensors did respond *in vivo*.

**Ratiometric imaging of subcellular NADPH level and NADH/NAD<sup>+</sup> ratio.** Prior to analyses, we validated two independent lines expressing each sensor. We tested different confocal laser powers to ensure that the laser power at 405 nm was sufficient and the illumination was not depleted by chlorophyll absorption. Raw  $R_{405/488}$  ratios obtained from 3-day-old seedlings of two independent iNAP and SoNar (cytosol, TKTP, and SRL) lines with different confocal laser powers indicated that, within the same tissues, the ratios were practically identical in all of the independent lines, with no statistically significant differences (Supplementary Fig. 5). These lines stably expressed sensors with different fluorescence intensities and thus different sensor concentrations in the same compartment, but different lines emitted similar ratios under untreated conditions. We selected the sensor lines with higher fluorescence intensities to use in our subsequent *in planta* studies (Line 1 for TKTP-iNAP4, cytosolic SoNar, and TKTP-SoNar and Line 2 for cytosolic iNAP1 and iNAP4-SRL,

respectively). Ratiometric analysis allows measurement of sensors independently of their expression levels, provided that there is a sufficient signal-to-noise ratio and little interference from any potential autofluorescence. The autofluorescence channel at the UV light spectra (405 nm excitation and  $450 \pm 17$  nm emission) was also set to exclude any potential interference from plant lignin autofluorescence throughout the experiment.

To assess the validity of the collected emission spectra for seedlings expressing iNAP and SoNar, we scanned the emission range for iNAP and SoNar from 424 to 599 nm in 10-day-old seedlings with 405 nm and 488 nm excitation, respectively (Supplementary Fig. 6). As all iNAP and SoNar sensors showed a characteristic emission peak at  $520 \pm 20$  nm, which was not seen in the WT, the fluorescence emission at  $520 \pm 20$  nm was significantly lower in the WT control without sensors. Due to the capacity of chloroplasts to absorb blue wavelength light, we tested different laser powers to avoid possible interference from chloroplasts (Supplementary Fig. 5). Chlorophyll absorption indeed interferes with the ratio measurement, and therefore the ratios in chlorophyll-containing tissues (e.g., shoots) cannot be compared with those in tissues with less or no chlorophyll (e.g., root). Nonetheless, the dynamic changes in the sensor ratios in the same compartment under various treatments (e.g., light or inhibitors) can be followed. Moreover, the circularly permuted yellow fluorescent protein-based iNAP sensors are pH sensitive when it is excited at 488 nm but not at 405 nm<sup>3,4</sup>, and it is almost certain that plants have numerous cation exchangers that are localized in different membranes and that may regulate pH changes across the organelles in response to stimuli. Thus, pH effects need to be carefully normalized, which can be done using the pH control sensor (iNAPc) in parallel experiments. We therefore included an iNAPc control for each subcellular compartment in all measurements to normalize the effects derived from pH interference and chlorophyll absorption (Supplementary Fig. 7).

To determine the redox ratios potentially that could be achievable by the sensors, we exogenously applied the oxidizing agents menadione and hydrogen peroxide ( $\text{H}_2\text{O}_2$ ) and the reducing agent dithiothreitol (DTT) by 5-min infiltration (Supplementary Fig. 8). Menadione and  $\text{H}_2\text{O}_2$  are broadly used to oxidize plant cells, and both mediate ROS formation through the catalytic transfer of electrons from endogenous donors to molecular oxygen. To assess whether these agents might affect the sensors directly, we first carried out an *in vitro* experiment. Although  $\text{H}_2\text{O}_2$  and menadione had no effect on the sensor ratios (Supplementary Fig. 8), DTT directly suppressed the ratios. Hence, only the *in planta* results for the oxidizing agents were shown. Menadione and  $\text{H}_2\text{O}_2$  significantly reduced the ratios of both iNAP sensors in all three compartments, indicating that the NADPH levels in these three compartments in the absence of oxidizing treatment were higher than the lowest detection ranges of the iNAP sensors. Menadione and  $\text{H}_2\text{O}_2$  treatments significantly lowered the SoNar ratio in plastid stroma but not in the cytosol (Supplementary Fig. 8), implying that the NADH/NAD<sup>+</sup> ratio is very low in the cytosol in darkness. In fact, a highly oxidized NAD(H) pool was determined in the cytosol of pea protoplasts<sup>33</sup> and the NADH/NAD<sup>+</sup> ratio was lower in the cytosol than the chloroplasts of barley protoplasts<sup>34</sup>. The ratios stimulated by illumination at  $296 \mu\text{mol m}^{-2} \text{s}^{-1}$  were used as controls (Supplementary Fig. 8). We also showed that L-ascorbic acid and reduced glutathione, which are abundant antioxidants in plant cells<sup>35</sup>, did not affect the ratios of the sensors in *in vitro* binding studies (Supplementary Fig. 9).

**Dynamic changes of NADPH and NADH/NAD<sup>+</sup> under illumination.** To examine the effect of light intensities, we compared the dynamic changes in subcellular pyridine nucleotides at two light intensities,  $40 \mu\text{mol m}^{-2} \text{s}^{-1}$  and  $296 \mu\text{mol m}^{-2} \text{s}^{-1}$ . We observed significant increases in stromal NADPH and NADH/NAD<sup>+</sup> and cytosolic NADH/NAD<sup>+</sup>, and decreases in cytosolic NADPH and peroxisomal NADPH, upon illumination at  $296 \mu\text{mol m}^{-2} \text{s}^{-1}$  (Fig. 2). However, at  $40 \mu\text{mol m}^{-2} \text{s}^{-1}$ , the NADPH ratiometric shift occurred only in stroma but not in the cytosol or peroxisome. In addition, both the stromal NADH/NAD<sup>+</sup> (Fig. 2e) and the cytosolic NADH/NAD<sup>+</sup> were more oxidized (Fig. 2d) at the lower light intensity than at the higher light intensity, indicating that the redox status of the NADH/NAD<sup>+</sup> pool in the cytosol is connected to that in the stroma. The stromal NADPH levels increased only after 60–90 s of illumination, reached a plateau after 120 s, and dropping quickly (within 30 s) after the light was withdrawn. Unlike the NADH/NAD<sup>+</sup> ratio in plastid stroma, which dropped below its basal level within 90 s after light withdrawal (Fig. 2e), the stromal NADPH level did not drop to the basal level, even after 4 min of darkness (Fig. 2b). These data imply that the CBB cycle is the major consumer of stromal NADPH, as Rubisco carboxylation stops at ~30 s after light withdrawal when the RuBP pool is exhausted<sup>36</sup>. Since NADP-MDH is active only under light<sup>14,24</sup>, whereas NAD-MDH is active in both light and dark conditions<sup>37</sup>, the malate-OAA shuttle in the chloroplasts can export only stromal NADH reducing equivalents but not stromal NADPH reducing equivalents in darkness (Fig. 2b, e). As the cytosolic NADH/NAD<sup>+</sup> pool was more oxidized than the stromal pool (Fig. 2d), a continuous export of NADH reducing equivalents, resulting in a stromal NADH/NAD<sup>+</sup> ratio even lower than that before illumination, was observed (Fig. 2e). All of the above changes were abolished by the application of the photosynthesis inhibitor DCMU (Fig. 2), due to its complete inhibition of the LEF (Supplementary Fig. 10b).

**Photorespiration is the main NADH contributor in mitochondria.** Since Arabidopsis GDC mutant is lethal<sup>38</sup>, we used aminoacetonitrile (AAN), an inhibitor of the mitochondrial conversion of glycine to serine and the production of NADH<sup>39</sup>, to investigate the contribution of photorespiration in supplying reducing equivalents. AAN does not affect photosynthesis in protoplasts under non-photorespiratory conditions (high  $\text{CO}_2$ ), thus supporting its specificity<sup>26</sup>. In the untreated control, illumination at  $296 \mu\text{mol m}^{-2} \text{s}^{-1}$  caused a drastic increase in stromal NADPH (Figs. 1b and 2b) and NADH/NAD<sup>+</sup> ratios (Fig. 2e) but a small decrease in both cytosolic (Figs. 1a and 2a) and peroxisomal NADPH (Figs. 1c and 2c). The cytosolic NADH/NAD<sup>+</sup> ratio was increased by illumination at  $296 \mu\text{mol m}^{-2} \text{s}^{-1}$ , but was decreased when the light intensity was only at  $40 \mu\text{mol m}^{-2} \text{s}^{-1}$  (Fig. 2d). When AAN was applied, however, even illumination at  $296 \mu\text{mol m}^{-2} \text{s}^{-1}$  failed to increase the stromal NADPH pool (Fig. 3a), and the NADH/NAD<sup>+</sup> ratio (Fig. 3b). By contrast, the production of stromal ATP (Fig. 3c), the electron transport rate (ETR) (Fig. 4k) and the respiration and photosynthesis rates (Supplementary Fig. 10) could still be detected. A pH increment in mitochondrial matrix was still detected in AAN-treated mitochondria (Fig. 3d), indicating that AAN does not interfere with the mETC machinery and gradient formation during electron transport. In addition to inhibitor studies, we further simulated a non-photorespiratory condition by including 10 mM  $\text{NaHCO}_3$  in the half-strength Murashige and Skoog medium during confocal analysis. Similar to the results of AAN treatment, when  $\text{NaHCO}_3$  was applied, illumination at  $296 \mu\text{mol m}^{-2} \text{s}^{-1}$  failed to increase the stromal NADPH pool (Fig. 3h), and the NADH/NAD<sup>+</sup> ratio (Fig. 3i). These results showed that stromal NADPH did not build up when the mitochondria failed to generate NADH by photorespiration.

Under normal conditions, illumination at  $296 \mu\text{mol m}^{-2} \text{s}^{-1}$  caused an increase in the cytosolic NADH/NAD<sup>+</sup> ratio (Fig. 2d) and a decrease in the cytosolic NADPH level (Fig. 2a); however, when photorespiration was prevented by AAN, illumination at  $296 \mu\text{mol m}^{-2} \text{s}^{-1}$  transiently increased the cytosolic NADH/NAD<sup>+</sup> (Fig. 3e), but the decrease in the cytosolic NADPH level became smaller (Fig. 3f). Yet, this effect did not occur at  $40 \mu\text{mol m}^{-2} \text{s}^{-1}$  (Fig. 3e, f). Although we were unable to target the SoNar sensor to peroxisomes, we showed that illumination at  $296 \mu\text{mol m}^{-2} \text{s}^{-1}$  caused a decrease in NADPH level in peroxisomes (Figs. 1c and 2c). This decrease did not occur under  $40 \mu\text{mol m}^{-2} \text{s}^{-1}$  illumination, probably because the rate of photorespiration increased with light intensity. When photorespiration was inhibited by AAN, no decreases in peroxisomal NADPH was seen (Fig. 3g).

Together, these results imply that during photorespiration, a large amount of NADH is generated in the mitochondria through the action of GDC, and concurrently, a large amount of NADH is oxidized in the peroxisomes through the action of HPR. The cytosol is thus in the path of the flow of reducing equivalents between chloroplasts, peroxisomes and mitochondria. The change in the cytosolic NADH/NAD<sup>+</sup> ratio thus reflects the flow of reducing equivalents between these three organelles.

#### Effects of mETC inhibitors on the flow of reducing equivalents.

Next, we examined the effects of mETC inhibitors, namely rotenone (complex I), TTFA (complex II), antimycin A (complex III), KCN (cytochrome *c*-dependent respiration), and oligomycin A (ATP synthase), on the NADPH and NADH/NAD<sup>+</sup> levels in different subcellular compartments (Fig. 4 and Supplementary Fig. 11). The use of rotenone, TTFA, AA, KCN, and oligomycin A increased the cytosolic SoNar ratios, but DCMU and AAN had no effect (Fig. 4, Supplementary Fig. 11). This was also true for

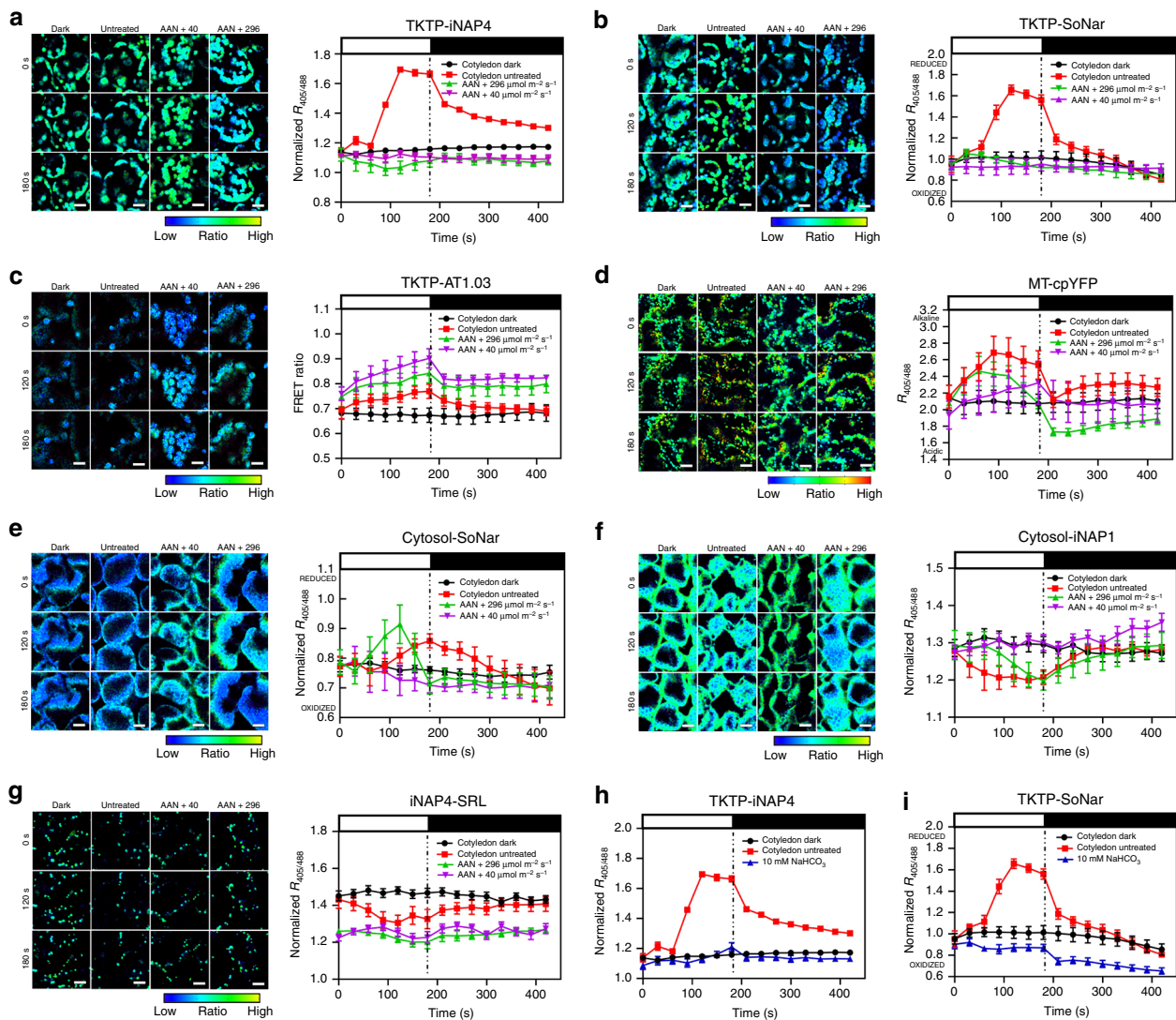


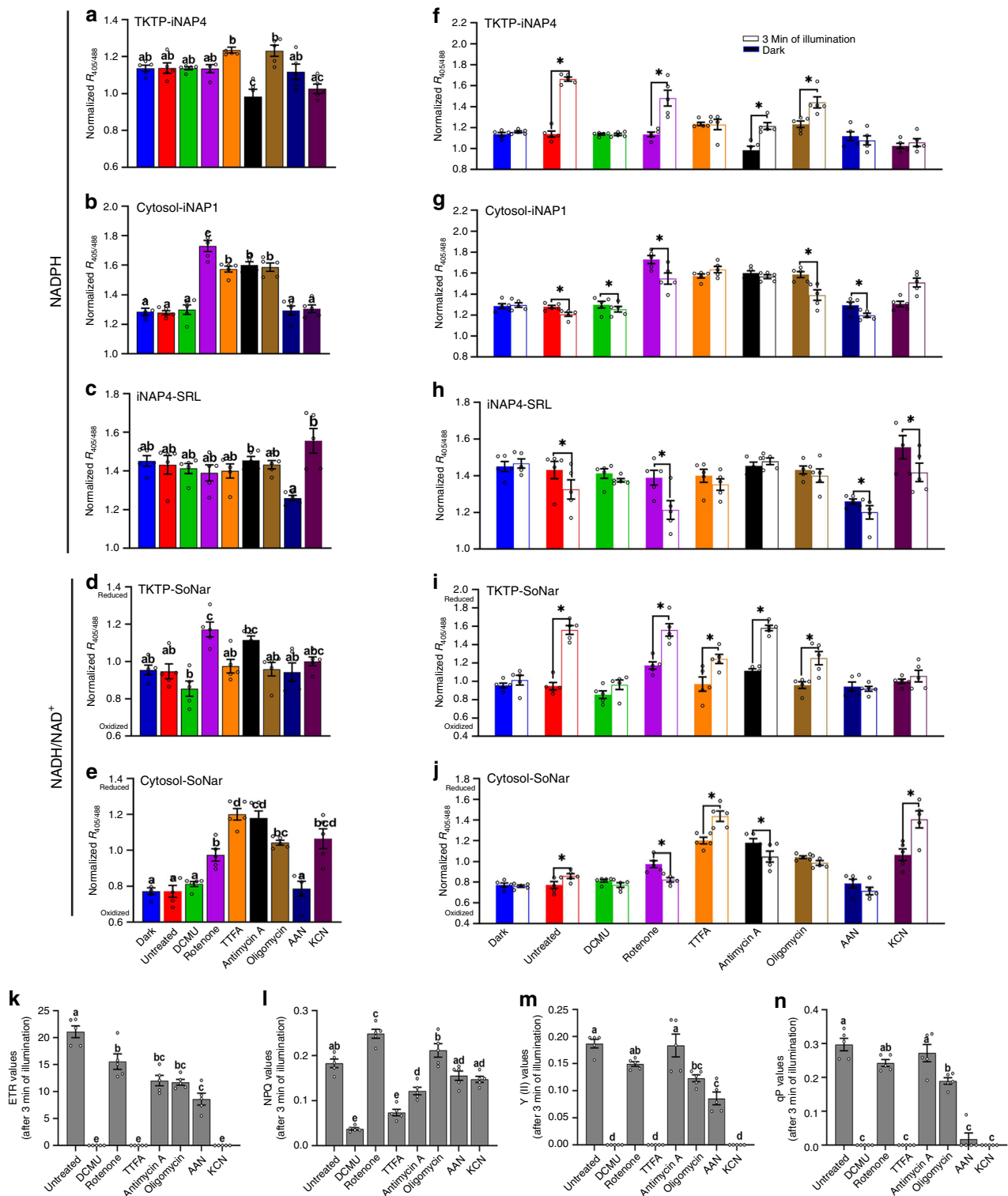
**Fig. 3** Dynamic changes of NADPH level, NADH/NAD<sup>+</sup> ratio, MgATP<sup>2-</sup> ratio, and pH level in 10-day-old seedlings pre-treated with aminoacetonitrile [AAN] or NaHCO<sub>3</sub>. The normalized ratiometric shifts of seedlings pre-treated with 18 mM AAN carrying **a** stromal iNAP4, **b** stromal SoNar, **c** stromal AT1.03, **d** mitochondrial matrix cpYFP, **e** cytosolic SoNar, **f** cytosolic iNAP1, and **g** peroxisomal iNAP4 in cotyledon in response to illumination for an interval of 30–180 s at 296  $\mu\text{mol m}^{-2} \text{s}^{-1}$ , or 40  $\mu\text{mol m}^{-2} \text{s}^{-1}$ , are shown. The normalized ratiometric shifts of seedlings in in half-strength Murashige and Skoog medium containing 10 mM NaHCO<sub>3</sub> carrying **h** stromal iNAP4, **i** stromal SoNar and illuminated at 296  $\mu\text{mol m}^{-2} \text{s}^{-1}$  are also shown. The illumination period is indicated by white bars and the values under the black bars represent data obtained after light withdrawal at 180 s ( $n = 5$ ; error bars  $\pm$  SEM). Scale bars, 20  $\mu\text{m}$ . All iNAP and SoNar results presented were normalized with cytosol-iNAPc, TKTP-iNAPc, and iNAPc-SRL, respectively.

cytosolic iNAP1 (except with KCN). This indicates that when the ability of mitochondria to consume NADH in darkness is inhibited, NADH and NADPH accumulate in the cytosol. However, the use of these inhibitors did not increase the basal NADPH level in chloroplasts, indicating that the stromal pool of NADPH in darkness is not affected by mETC activity, probably because stromal NADP-MDH is a light-dependent enzyme. In addition, the basal level of stromal NADH/NAD<sup>+</sup> ratio was significantly increased by rotenone application, suggesting that reducing equivalents accumulate in the cytosol and stroma after the inhibition of complex I (Fig. 4d).

Upon illumination, an increment in stromal NADPH in seedlings treated with rotenone, AA, and oligomycin A can still be clearly seen (Fig. 4f), as these inhibitors do not inhibit the LEF in chloroplasts. However, TTFA treatment completely suppressed the accumulation of stromal NADPH upon illumination (Fig. 4f) and ETR, Y(II) and qP (Fig. 4k, m, n),

probably because TTFA suppresses ferredoxin: NADP<sup>+</sup> oxidoreductase (FNR)<sup>40</sup>, and reduced the photosynthesis rate (Supplementary Fig. 10b). In addition, we still observed an increase in stromal NADH/NAD<sup>+</sup> in seedlings treated with rotenone, TTFA and AA upon illumination (Fig. 4i). Surprisingly, rotenone and AA treatments resulted in a decrease in cytosolic NADH/NAD<sup>+</sup> ratio upon illumination (Fig. 4j), possibly due to de novo NAD<sup>+</sup> synthesis.

Furthermore, a study with the respiratory inhibitor KCN, as a mean to elucidate the reducing equivalent dynamics in cytochrome *c*-dependent respiration, revealed that KCN treatment also completely inhibited ETR (Fig. 4k). When KCN was applied, the basal cytosolic NADH/NAD<sup>+</sup> ratio was higher in darkness. In the presence of KCN, whereas illumination did not increase the stromal NADPH (Fig. 4f) or NADH/NAD<sup>+</sup> ratio (Fig. 4i), it did increase the cytosolic NADPH (Fig. 4g) and NADH/NAD<sup>+</sup> ratio (Fig. 4j).



**Discussion**

Monitoring real-time subcellular dynamic changes in reducing equivalents *in planta* has been a long-term challenge. The iNAP and SoNar fluorescence-based sensors were initially introduced in mammalian cells to study the responsiveness of reducing equivalents in homeostasis and cancer cells *in vivo*<sup>3,4</sup>. SoNar is preferred over another NADH/NAD<sup>+</sup> sensor, Peredox-mCherry, because it has a 10-fold higher dynamic range and does not aggregate in the cytosol<sup>41</sup>. For the first time, we introduced these iNAP and SoNar sensors into several subcellular compartments

in plants (Supplementary Fig. 1). This *in planta* imaging has resolved the bottleneck preventing the study of physiological changes in reducing equivalents at the subcellular level, providing a valuable tool to monitor the real-time dynamics of reducing equivalents without destroying the plant tissues.

We introduced two iNAP sensors with high (iNAP1) and low (iNAP4) NADPH affinities into chloroplasts, peroxisomes and cytosol of Arabidopsis. Our data indicated that iNAP1 is more suitable for observing the changes in cytosolic NADPH levels, whereas iNAP4 is more suitable for monitoring the changes in

**Fig. 4 Effects of various inhibitors on the light responses of NADPH levels and NADH/NAD<sup>+</sup> ratios in 10-day-old seedlings.** The inhibitors used were 0.02 mM 3-(3,4-dichlorophenyl)-1,1-dimethylurea (DCMU), 0.05 mM rotenone, 0.1 mM thenoyltrifluoroacetone (TTFA), 0.01 mM antimycin A, 0.01 mM oligomycin; 18 mM aminoacetonitrile (AAN), and 0.5 mM potassium cyanide (KCN). **a–e** Normalized  $R_{405/488}$  ratios of **a** stromal iNAP4, **b** cytosolic iNAP1, **c** peroxisomal iNAP4, **d** stromal SoNar, and **e** cytosolic SoNar. Different letters indicate significant differences as analyzed by Tukey's HSD test ( $P < 0.05$ ) ( $n = 5$ ; error bars  $\pm$  SEM). **f–j** Ratiometric shifts of normalized  $R_{405/488}$  ratios of **f** stromal iNAP4, **g** cytosolic iNAP1, **h** peroxisomal iNAP4, **i** stromal SoNar, and **j** cytosolic SoNar in the cotyledon of 10-day-old seedlings in response to illumination at  $296 \mu\text{mol m}^{-2} \text{s}^{-1}$  for 180 s are presented as empty bars, while the initial point (0 s) is presented as filled color bars. Asterisks indicate significant differences ( $P < 0.05$ ) before and after 3 min of illuminations as determined by paired *t*-test ( $n = 5$ ; error bars  $\pm$  SEM). All results were normalized with TKTP-INAPc. **k–n** Effects of various inhibitors on **k** electron transport reaction (ETR), **l** non-photochemical quenching (NPQ), **m** effective PS II quantum yield (Y(II)), and **n** coefficient of photochemical quenching (qP). Data from cotyledon in response to illumination for up to 180 s at  $280 \mu\text{mol m}^{-2} \text{s}^{-1}$  are presented. Different letters indicate significant differences analyzed by Tukey's HSD test ( $P < 0.05$ ) ( $n = 5$ ; error bars  $\pm$  SEM).

chloroplast and peroxisome NADPH levels, implying that the cytosolic NADPH concentration may be lower in the cytosol than in the other two compartments. These data corroborate results from past experiments involving the rapid fractionation of illuminated barley protoplasts into chloroplasts and cytosol, in which the total concentrations of NADP<sup>+</sup> and NADPH were estimated to be 0.6–0.8 mM in chloroplasts and 0.25–0.35 mM in cytosol, when the NADPH/NADP<sup>+</sup> ratios in these two compartments (1.4 and 1.5) were similar under limiting CO<sub>2</sub> conditions<sup>42</sup>.

De novo synthesis of NADP<sup>+</sup> in cytosol, chloroplasts, and peroxisomes is carried out by the ATP-dependent NAD kinases: NADK1, NADK2, and NADK3<sup>43</sup>, among which NADK2 in chloroplasts, is a light-dependent enzyme<sup>44</sup>. Illumination of 3-week-old plants for 5 min to 1 h gradually increases the NADP<sup>+</sup> and NADPH pools in the rosette leaves of WT plants but not in a *nadk2* mutant, indicating that, under illumination, the synthesis of NADP<sup>+</sup> from NAD<sup>+</sup> by NADK2 in the chloroplasts is the major NADP<sup>+</sup> synthesis pathway. The newly synthesized NADP<sup>+</sup> is then reduced to NADPH by FNR, and the NADPH/NADP<sup>+</sup> ratio is maintained at  $\sim 1$  in the first 5 min of illumination, and gradually decreases to  $\sim 0.7$  after 60 min of illumination<sup>44</sup>.

By using iNAP sensors with different affinities, we observed not only an increase in stromal NADPH, but also a small decrease of NADPH in the cytosol and peroxisomes upon illumination (Fig. 2). As reported previously from barley leaf protoplast experiments, the stromal NADPH/NADP<sup>+</sup> ratio declines within 30 s in darkness after illumination<sup>24</sup>; similarly, we observed a rapid decline in stromal NADPH and NADH/NAD<sup>+</sup> ratio after the light was turned off (Fig. 2). The rapid decline of NADPH level in the first 30 s of darkness can be mainly attributed to the CBB cycle, as Rubisco carboxylation stops  $\sim 30$  s after light withdrawal<sup>36</sup>. After that, the decline might be mainly due to the malate-OAA shuttle. A small amount of NADPH may also be recycled to NADP<sup>+</sup> in the light by light-dependent glutathione reductase, but the flux is expected to be small because the substrate, GSSG, is present in the low nanomolar range<sup>35</sup>. Although NAD<sup>+</sup> can be transported through chloroplasts, mitochondria, and peroxisomes via NDT1, NDT2<sup>45</sup>, and PXN<sup>46</sup>, organelle membranes are impermeable to NADP(H) and NADH due to the lack of transporters. This enables the subcellular compartmentation of NADP(H) and NAD(H) and requires their indirect translocation between subcellular compartments by shuttles, such as the malate-OAA shuttle.

The operation of the malate-OAA shuttle requires the presence of various MDHs in different compartments. Arabidopsis possesses two chloroplastic MDHs, the light-dependent NADP<sup>+</sup>-specific MDH and the light-independent NAD<sup>+</sup>-specific MDH, both of which could transfer stromal surplus reducing equivalents to malate. Our data showed that the post-illumination decrease in stromal NADPH was slower than the drop in stromal NADH/NAD<sup>+</sup> ratio after 30 s of darkness (Fig. 2), consistent with the natures of these two classes of plastidic MDHs. NADPH is

important for fatty acid synthesis and detoxification of oxidative stresses in chloroplasts in the light<sup>47</sup>. This may provide an explanation of why, during evolution, two plastidic MDHs with different substrate specificity and light dependence have been maintained in the plant genomes. During photosynthesis, the surplus NADPH must be exported by the malate-OAA shuttle and therefore requires an active NADP-MDH that functions in a light-dependent manner. In darkness, malate accumulated in the light can be converted to NADH by NAD-MDHs in various subcellular compartments, but not by NADP-MDH to NADPH in plastids.

Fundamental to our study was the question of what serves as the major source of reducing equivalents to mETC during photosynthesis. A key insight from our AAN and NaHCO<sub>3</sub> experiments was that in the absence of photorespiration, the increases in stromal NADPH and NADH/NAD<sup>+</sup> upon illumination disappeared (Fig. 3a, b, h, i), suggesting that when photorespiration fails to generate NADH in mitochondria, the mitochondrial malate-OAA shuttle can supply NADH to the mETC (Fig. 3d). This, in turn, could indirectly draw reducing equivalents from the chloroplasts through the cytosolic malate pool and chloroplastic malate-OAA shuttle (Fig. 5). Hence, illumination upon AAN and NaHCO<sub>3</sub> treatments caused no increase in stromal NADPH (Fig. 3a, h). Our data imply that during photosynthesis, the amount of NADH generated by the photorespiratory GDC is higher than the NADH-dissipating capacity of mitochondria including those of complex I, non-proton-pumping internal NADH dehydrogenases (NDA1 and NDA2), and the mETC and therefore a net export of malate is expected. GDC is the most abundant soluble enzyme in the mitochondria of photosynthetic tissues, and GDC activity increases significantly only after the chloroplasts are mature enough to carry out photosynthesis<sup>48</sup>. Although GDC is highly abundant, the amount of NADH generated by GDC is dependent on the size of the flux of photorespiration cycle, which is dependent on the light intensity. When AAN or NaHCO<sub>3</sub> were supplied, we detected no increase in stromal NADPH level (Fig. 3a, h) or NADH/NAD<sup>+</sup> ratio (Fig. 3b, i).

It has been estimated that only 5% of NADPH generated from the LEF in chloroplasts is exported by the malate valve<sup>15</sup>. This implies that when photorespiration does not generate any NADH in mitochondria, in addition to the tricarboxylic acid (TCA) cycle which could supply an unknown amount of reducing equivalents, the mitochondrial ETC can rely on the import of malate for NADH supply. However, under normal photorespiratory conditions, when copious NADH is produced in mitochondria, the peroxisomes could consume NADH at a theoretical ratio of 1:1. In reality, photorespiration is also a source of serine synthesis<sup>49</sup>, and therefore the ratio of mitochondrial NADH production and peroxisomal NADH consumption is  $>1$ <sup>8</sup>. As chloroplasts also export malate, it builds up during the day, and most is stored in the vacuole<sup>17</sup>. This indicates that at the whole-cell level, reducing equivalents accumulate during photosynthesis in the form of malate



are exported by the mitochondrial malate–OAA flux. (5) Some serine generated from photorespiration leaves the photorespiration pathway (S)<sup>9</sup>, and hence the amount of NADH consumed by HPR in the peroxisome is less than the amount of NADH generated by the GDC. (6) Around 5% of electrons generated from the LEF (L) in the form of NADPH are exported by the malate–OAA flux from the chloroplasts (f)<sup>15</sup>. (7) Malate accumulates during photosynthesis is stored in the vacuole. The rate of malate accumulation (M) is  $f + S - N$ , where  $N$  is the amount of NADH consumed by the cytosolic nitrate reductase during nitrogen assimilation. Hence, malate is basically derived from OAA, which is synthesized from PEP (P) and whose input is also equal to  $f + S - N$ . (8) Since LEF generates a higher NADPH/ATP ratio than the ratio consumed by the CBB, surplus NADPH is generated during photosynthesis, and though some is exported to extrachloroplastic compartments through the malate–OAA shuttle, a build-up of stromal NADPH occurs (Fig. 2b). After photorespiration is inhibited by AAN or NaHCO<sub>3</sub> (Fig. 5b), the following assumptions hold: (1) Since no NADH is generated by GDC in the mitochondria ( $R = 0$ ), malate, instead of being exported, is imported into mitochondria to supply NADH to the mETC. (2) As the cytosolic malate/OAA ratio decreases, the malate–OAA flux (F) of the chloroplasts increases and exports reducing equivalents from stromal NADPH at a higher rate. As a result, no increase in NADPH concentration occurs (Fig. 3b). (3) The net synthesis of malate (m) is therefore equal to  $F - E - n$ , which is significantly smaller than the  $M (f + S - N)$  in the absence of AAN treatment. Hence, the reversible reaction between malate and OAA helps to build up the equilibrium of reducing equivalents between subcellular compartments under light and dark conditions.

## Methods

**Plasmid construction and generation of plant lines.** To construct the plant transformation vectors, the cDNAs of iNAP1, iNAP4, iNAPc, and SoNar were amplified with Platinum Pfx polymerase (Invitrogen) from the pcDNA3.1 vectors<sup>3</sup> and subcloned into the BamHI and XbaII restriction sites of a modified Gateway pENTR/D-TOPO vector (Invitrogen). For targeting to plastids, peroxisomes, and mitochondria, the sequences from *Nicotiana tabacum* chloroplast transketolase transit peptide (TKTP)<sup>59</sup>, peroxisomal targeting signal type 1 (SRL)<sup>60</sup> or mitochondrial-targeting sequence from *Nicotiana plumbaginifolia*  $\beta$ -ATPase (MT)<sup>31</sup> were fused to the N-terminus (TKTP and MT) or C-terminus (SRL) of the sensor proteins, respectively. Their unfused versions were used for cytosolic targeting. The cDNAs were then transferred into the recipient plant transformation pEarleyGate100 vector<sup>61</sup> under the control of the CaMV35S promoter. The pEarleyGate100 vectors were transformed into *Arabidopsis thaliana* plants (ecotype Columbia, Col-0) using the floral dip method<sup>62</sup>. Positive transformants were screened using fluorescence microscopy (Nikon Eclipse 80i). The sensor cDNA sequences were also fused downstream to the 6xHis-tag of the pRSETb vector for protein expression in *Escherichia coli* using the BamHI and HindIII sites. Primer sequences are listed in Supplementary Table 1. All constructs were confirmed by nucleotide sequencing. Furthermore, WT (Col-0) seedlings carrying pH2GW7-MT-cpYFP (mitochondrial matrix pH sensor) and pEarleyGate100-TKTP-AT1.03 (stromal MgATP<sup>2-</sup> sensor) were as previously reported<sup>2,30,63</sup>.

**Plant cultivation.** The transformed plants were germinated and cultivated on plates containing Murashige and Skoog medium<sup>64</sup> supplemented with 2% (w/v) sucrose and 1% (w/v) Phytigel and stratified for 2 days at 4 °C in darkness before being transferred to a long-day condition with a photoperiod of 16 h at 120–150  $\mu\text{mol photon m}^{-2} \text{s}^{-1}$  at 22 °C and 8 h in darkness at 18 °C. Unless otherwise stated, for assay purposes, all seedlings were adapted in darkness for 1 h before image acquisition.

**Recombinant protein expression and purification.** *Escherichia coli* BL21 (DE3) pLys cells carrying the pRSETb iNAP1, iNAP4, iNAPc, and SoNar plasmids were grown in 15 ml LB medium containing 100  $\mu\text{g/ml}$  carbenicillin at 37 °C until the cultures reached OD<sub>600</sub> of 0.6. The expression of His-tagged proteins were induced by 0.1 mM isopropyl  $\beta$ -D-1-thiogalactopyranoside (IPTG), and the cells were then transferred to 18 °C for another 16 h of growth. Cells were collected by centrifugation at 4000 $\times$ g for 30 min at 4 °C, and the cell pellets were suspended in ice-cold buffer A (20 mM sodium phosphate buffer, pH 7.4, containing 0.5 M sodium chloride, 40 mM imidazole, and cComplete protease inhibitor cocktail (Roche)).

After sonication, the lysates were fractionated by centrifugation at 16,000  $\times$ g for 5 min at 4 °C. The supernatants were loaded into a 1-ml HisTrap<sup>TM</sup> FF column (GE Healthcare) with a syringe attached to a 0.45- $\mu\text{m}$  filter. After being washed with 2 column volumes of buffer A, proteins were eluted from the resin using buffer B (20 mM sodium phosphate buffer, pH 7.4, containing 0.5 M sodium chloride and 400 mM imidazole). The recombinant proteins were then dialyzed in dialysis buffer (20 mM Tris-HCl, pH 7.5, and 150 mM sodium chloride) overnight and stored at –80 °C before assay. The elutes were separated by 10% (w/v) SDS-PAGE and stained with Coomassie blue dye. NativeMark<sup>TM</sup> unstained protein standard (Invitrogen) was used as molecular weight marker. Expected molecular masses of 6xHis-tagged iNAP1, iNAP4, and iNAPc proteins were all 42.9 kDa.

**Confocal imaging and ratiometric image analysis.** Confocal imaging of seedling was set up as previously described<sup>65</sup>. Imaging was performed with 5 $\times$  and 40 $\times$  oil-immersion lenses in multitrack mode using a Zeiss LSM710 NLO confocal microscope (Carl Zeiss Microscopy). Plants expressing iNAP1, iNAP4, and iNAPc in various subcellular compartments were excited sequentially at 405 nm and 488 nm, and emission was detected at  $520 \pm 16$  nm.  $R_{\text{iNAP}}$ ,  $R_{\text{iNAPc}}$ , and  $R_{\text{SoNar}}$  represent the raw ratios of emission excited at 405 nm and 488 nm for iNAP1/4, iNAPc, and SoNar. Autofluorescence was recorded at 431–469 nm and chlorophyll fluorescence was collected at 629–700 nm.

Confocal images were processed with a custom MATLAB-based analysis suite<sup>66</sup>. The ratiometric images were analyzed on a pixel-by-pixel basis using  $x$ ,  $y$  noise filtering, and fluorescence background subtraction was conducted based on the intensity of the cell samples not expressing sensors from the dark side of the images. Visually, all the ratio profiles in the mesophyll were displayed in pseudocolors. iNAPc is the pH control sensor of iNAP and SoNar<sup>3</sup>. The pH-corrected ratio (normalized  $R_{405/488}$ ) was calculated with the formula below,

$$\text{Normalized } R_{405/488} = R_{\text{iNAP or SoNar}} / R_{\text{iNAPc}}$$

**Protoplast isolation and transfection.** Isolation of mesophyll protoplasts from the leaves of 28-day-old Arabidopsis plants expressing iNAP4-SRL or iNAPc-SRL was carried out as previously described<sup>67</sup>. The pBI221-mRFP-SRL plasmid was a kind gift from Prof. Liwen Jiang of the Chinese University of Hong Kong. Recombinant plasmids were isolated using MAGEN HiPure Plasmid EF Midi Kit. DNA concentration was adjusted to 600  $\text{ng } \mu\text{l}^{-1}$  per 5 kb of DNA. A total of 200  $\mu\text{l}$  protoplast solution was mixed with 10  $\mu\text{l}$  of recombinant plasmid and incubated in darkness at room temperature overnight before acquisition by confocal microscopy.

**In vitro and semi in vivo characterization of iNAP and SoNar.** To characterize the sensors, both in vitro and semi in vivo methods were adopted. To determine the in vitro  $K_d$  of the recombinant sensors at room temperature, NADPH, NADP<sup>+</sup>, NADH, and NAD<sup>+</sup> nucleotides were titrated for iNAP1, iNAP4, iNAPc, and SoNar at pH 7.2, 7.5, 8.1, and 8.4, respectively. Nucleotide concentrations were fixed at 0  $\mu\text{M}$ , 2  $\mu\text{M}$ , 10  $\mu\text{M}$ , 25  $\mu\text{M}$ , 50  $\mu\text{M}$ , 100  $\mu\text{M}$ , 125  $\mu\text{M}$ , 250  $\mu\text{M}$ , 500  $\mu\text{M}$ , and 1000  $\mu\text{M}$ . The purified recombinant sensor proteins were diluted in pseudocytosol medium supplemented with 100 mM potassium gluconate, 30 mM NaCl, 25 mM MES, 25 mM HEPES, 40% sucrose, and 1  $\text{mg ml}^{-1}$  (w/v) BSA (pH 7.5) to a final concentration of 0.5  $\mu\text{M}$ . Each assay was performed with 50  $\mu\text{l}$  nucleotides and 50  $\mu\text{l}$  protein arrayed in 96-well black plates (Corning Costar). Fluorescence characteristics of purified iNAP1, iNAP4, iNAPc, and SoNar were detected by a multimode reader (Victor X3, PerkinElmer) with sequential dual excitation at 405 nm and 485 nm, whereas emission was detected at 520 nm.

For semi in vivo experiment, 6–7-day-old seedlings were infiltrated with 100  $\mu\text{M}$  digitonin buffer supplemented with 100  $\mu\text{M}$  digitonin, 100 mM potassium gluconate, 1 mM MgCl<sub>2</sub>, 5 mM EGTA, and 10 mM HEPES, and pH 7.5. Seedlings containing cytosolic sensors were then infiltrated in the buffer with different NADPH concentrations (0  $\mu\text{M}$ , 0.1  $\mu\text{M}$ , 1.0  $\mu\text{M}$ , 4.0  $\mu\text{M}$ , 8.0  $\mu\text{M}$ , 10.0  $\mu\text{M}$ , 25.0  $\mu\text{M}$ , 50.0  $\mu\text{M}$ , 100.0  $\mu\text{M}$ , and 500.0  $\mu\text{M}$  for iNAP) or a total concentration of 100  $\mu\text{M}$  NADH/NAD<sup>+</sup> of different ratios (for SoNar) in pseudocytosol medium for 5 min before imaging.

**Responses of sensors to oxidants, reductant, and antioxidants.** To obtain the potential redox ratios of the sensor lines in vitro and in planta, purified iNAP or SoNar recombinant proteins and 10-day-old seedlings were either treated with 10 mM dithiothreitol (DTT) or oxidized with 10 mM H<sub>2</sub>O<sub>2</sub> or 30  $\mu\text{M}$  menadione. 10 mM L-ascorbic acid or 10 mM reduced glutathione were also tested via in vitro study. Purified recombinant proteins were diluted in pseudocytosol medium as described above. Seedlings were infiltrated for 5 min in half-strength Murashige and Skoog medium with or without reagents before imaging.

**Light intensity analysis.** Seedlings were cultivated as described above. To explore the effect of light intensity, seedlings were exposed to different light intensities (40  $\mu\text{mol m}^{-2} \text{s}^{-1}$  or 296  $\mu\text{mol m}^{-2} \text{s}^{-1}$  using confocal microscope equipped with a halogen lamp (HAL 100 W; Philips). The light intensity of confocal microscope halogen lamp (HAL 100 W; Philips) was determined using a Lutron LX-120 light meter (Lutron, Taipei, Taiwan) and converted into  $\mu\text{mol m}^{-2} \text{s}^{-1}$  using the formula

as previously described<sup>68</sup>. Each step took 30 s of illumination and imaging was immediately captured after each illumination period. After 3 min with 30 s intervals of exposure to the light, relaxation of seedlings in darkness was monitored for 4 min, during which the images were acquired every 30 s. Light intensity response curves for compartmentalized iNAP1 and iNAP4 were normalized by iNAPc.

**Inhibitors treatment.** Ten-day-old seedlings were infiltrated for 5 min in half-strength Murashige and Skoog medium with or without inhibitors. The following inhibitors were prepared and used to treat the seedlings in this study: inhibitors of photosynthesis (0.02 mM DCMU), mitochondrial complex I (0.05 mM rotenone), SDH (0.1 mM TTFA), complex III (0.01 mM antimycin A), complex IV (0.5 mM KCN), mitochondrial ATP synthase (0.01 mM oligomycin A)<sup>2</sup>, and photorespiration (18 mM AAN<sup>69</sup> and 10 mM NaHCO<sub>3</sub><sup>70</sup>). Unless otherwise stated, after infiltration, all seedlings were incubated in the dark for 1 h before imaging. The 10-day-old pretreated seedlings were illuminated at 296  $\mu\text{mol m}^{-2} \text{s}^{-1}$ .

**Determination of oxygen consumption rate at room temperature.** Respiratory oxygen consumption and photosynthetic oxygen evolution rate were measured with a Clark-type electrode (Oxygraph plus, Hansatech). Measurements were performed with 0.025 g of 10-day-old seedlings. Following an initial dark equilibration of the seedlings, oxygen was measured in the dark for 4 min before the seedlings were illuminated at an intensity of 296  $\mu\text{mol m}^{-2} \text{s}^{-1}$  for 3 min at room temperature and then subjected to 3 min of darkness. The consumption or evolution rate was determined for each minute interval. The oxygen levels from the fifth to sixth and eighth to ninth minutes were used to calculate the evolution rate and consumption rate (nanomoles of O<sub>2</sub> per second), respectively. The rate of photosynthesis was calculated as the evolution rate minus consumption rate. The respiration rate (%) was calculated as follows,

$$\text{Respiration rate (\%)} = \frac{\frac{\text{oxygen consumption rate (treated seedlings)}}{\text{total seedling fresh weight (g)}}}{\text{oxygen consumption rate (untreated seedlings)}} \times 100$$

**Determination of chlorophyll fluorescence parameters.** Fluorescence parameters were measured with a chlorophyll fluorometer (MAXIPAM, Heinz Walz) at room temperature. Treated seedlings were incubated in darkness for 1 h. The fluorescence yield was then measured with actinic light at 280  $\mu\text{mol m}^{-2} \text{s}^{-1}$  at interval of 30 s up to 3 min in the presence or absence of inhibitors, and following by 4 min of darkness. The effective quantum yield (Y(II)), non-photochemical quenching (NPQ), and photochemical quenching (qP) were calculated as  $[(F_m' - F_0)/F_m']$ ,  $[(F_m - F_m')/F_m']$ , and  $[(F_m' - F_0)/(F_m' - F_0)]$ , respectively.

**Data analysis.** All data are shown as the means with standard error (mean  $\pm$  SEM). The collected data were analyzed for statistical significance using analysis of variance (Tukey's HSD) and paired *t*-test at  $P < 0.001$ ,  $P < 0.01$ , and  $P < 0.05$  by SPSS (Version 20).

**Reporting summary.** Further information on research design is available in the Nature Research Reporting Summary linked to this article.

## Data availability

We declare that the main data supporting the findings of this study are available within the article and its Supplementary Information files. Source data are provided with this paper. Extra data are available from the corresponding author upon request.

Received: 10 January 2020; Accepted: 9 June 2020;

Published online: 26 June 2020

## References

- Liang, C. et al. Impacts of high ATP supply from chloroplasts and mitochondria on the leaf metabolism of *Arabidopsis thaliana*. *Front. Plant Sci.* **6**, 922 (2015).
- Voon, C. P. et al. ATP compartmentation in plastids and cytosol of *Arabidopsis thaliana* revealed by fluorescent protein sensing. *Proc. Natl. Acad. Sci. USA* **115**, E10778–E10787 (2018).
- Tao, R. K. et al. Genetically encoded fluorescent sensors reveal dynamic regulation of NADPH metabolism. *Nat. Methods* **14**, 720–728 (2017).
- Zhao, Y. Z. et al. SoNar, a highly responsive NAD<sup>+</sup>/NADH sensor, allows high-throughput metabolic screening of anti-tumor agents. *Cell Metab.* **21**, 777–789 (2015).
- Erb, T. J. & Zarzycki, J. A short history of RubisCO: the rise and fall (?) of Nature's predominant CO<sub>2</sub> fixing enzyme. *Curr. Opin. Biotechnol.* **49**, 100–107 (2018).
- Sharkey, T. D. Photorespiration. *eLS* <https://doi.org/10.1038/npg.els.0001292>, (2001).
- Bauwe, H., Hagemann, M. & Fernie, A. R. Photorespiration: players, partners and origin. *Trends Plant Sci.* **15**, 330–336 (2010).
- Busch, F. A., Sage, R. F. & Farquhar, G. D. Plants increase CO<sub>2</sub> uptake by assimilating nitrogen via the photorespiratory pathway. *Nat. Plants* **4**, 46–54 (2018).
- Abadie, C., Boex-Fontvieille, E. R., Carroll, A. J. & Tcherkez, G. In vivo stoichiometry of photorespiratory metabolism. *Nat. Plants* **2**, 15220 (2016).
- Selinski, J. & Scheibe, R. Malate valves: old shuttles with new perspectives. *Plant Biol.* **21**, 21–30 (2019).
- Allen, J. F. Cyclic, pseudocyclic and noncyclic photophosphorylation: new links in the chain. *Trends Plant Sci.* **8**, 15–19 (2003).
- Kramer, D. M. & Evans, J. R. The importance of energy balance in improving photosynthetic productivity. *Plant Physiol.* **155**, 70–78 (2011).
- Voon, C. P. & Lim, B. L. ATP translocation and chloroplast biology. *Natl. Sci. Rev.* **6**, 1073–1076 (2019).
- Scheibe, R. NADP<sup>+</sup>-malate dehydrogenase in C-3-plants - regulation and role of a light-activated enzyme. *Physiol. Plant.* **71**, 393–400 (1987).
- Fridlyand, L. E., Backhausen, J. E. & Scheibe, R. Flux control of the malate valve in leaf cells. *Arch. Biochem. Biophys.* **349**, 290–298 (1998).
- Vishwakarma, A., Tetali, S. D., Selinski, J., Scheibe, R. & Padmasree, K. Importance of the alternative oxidase (AOX) pathway in regulating cellular redox and ROS homeostasis to optimize photosynthesis during restriction of the cytochrome oxidase pathway in *Arabidopsis thaliana*. *Ann. Bot.* **116**, 555–569 (2015).
- Gerhardt, R., Stitt, M. & Heldt, H. W. Subcellular metabolite levels in spinach leaves - regulation of sucrose synthesis during diurnal alterations in photosynthetic partitioning. *Plant Physiol.* **83**, 399–407 (1987).
- Yoshida, K., Terashima, I. & Noguchi, K. Up-regulation of mitochondrial alternative oxidase concomitant with chloroplast over-reduction by excess light. *Plant Cell Physiol.* **48**, 606–614 (2007).
- Noguchi, K. & Yoshida, K. Interaction between photosynthesis and respiration in illuminated leaves. *Mitochondrion* **8**, 87–99 (2008).
- Zakhartsev, M. et al. Metabolic model of central carbon and energy metabolisms of growing *Arabidopsis thaliana* in relation to sucrose translocation. *BMC Plant Biol.* **16**, 262 (2016).
- Zhao, Y. N. et al. Malate transported from chloroplast to mitochondrion triggers production of ROS and PCD in *Arabidopsis thaliana*. *Cell Res.* **28**, 448–461 (2018).
- Pastore, D., Trono, D., Laus, M. N., Di Fonzo, N. & Flagella, Z. Possible plant mitochondria involvement in cell adaptation to drought stress - a case study: durum wheat mitochondria. *J. Exp. Bot.* **58**, 195–210 (2007).
- Gardeström, P. & Wigge, B. Influence of photorespiration on ATP/ADP ratios in the chloroplasts, mitochondria, and cytosol, studied by rapid fractionation of barley (*Hordeum vulgare*) protoplasts. *Plant Physiol.* **88**, 69–76 (1988).
- Igamberdiev, A. U., Romanowska, E. & Gardeström, P. Photorespiratory flux and mitochondrial contribution to energy and redox balance of barley leaf protoplasts in the light and during light-dark transitions. *J. Plant Physiol.* **158**, 1325–1332 (2001).
- Cheung, C. Y., Poolman, M. G., Fell, D. A., Ratcliffe, R. G. & Sweetlove, L. J. A diel flux balance model captures interactions between light and dark metabolism during day-night cycles in C3 and crassulacean acid metabolism leaves. *Plant Physiol.* **165**, 917–929 (2014).
- Gardeström, P. & Igamberdiev, A. U. The origin of cytosolic ATP in photosynthetic cells. *Physiol. Plant.* **157**, 367–379 (2016).
- Lee, C. P., Eubel, H. & Millar, A. H. Diurnal changes in mitochondrial function reveal daily optimization of light and dark respiratory metabolism in *Arabidopsis*. *Mol. Cell. Proteom.* **9**, 2125–2139 (2010).
- Shameer, S., Ratcliffe, R. G. & Sweetlove, L. J. Leaf energy balance requires mitochondrial respiration and export of chloroplast NADPH in the light. *Plant Physiol.* **180**, 1947–1961 (2019).
- Kumakura, N. et al. SGS3 and RDR6 interact and colocalize in cytoplasmic SGS3/RDR6-bodies. *FEBS Lett.* **583**, 1261–1266 (2009).
- Schwarzlander, M., Logan, D. C., Fricker, M. D. & Sweetlove, L. J. The circularly permuted yellow fluorescent protein cpYFP that has been used as a superoxide probe is highly responsive to pH but not superoxide in mitochondria: implications for the existence of superoxide 'flashes'. *Biochem. J.* **437**, 381–387 (2011).
- Logan, D. C. & Leaver, C. J. Mitochondria-targeted GFP highlights the heterogeneity of mitochondrial shape, size and movement within living plant cells. *J. Exp. Bot.* **51**, 865–871 (2000).
- Zhao, Y. Z. et al. In vivo monitoring of cellular energy metabolism using SoNar, a highly responsive sensor for NAD(+)/NADH redox state. *Nat. Protoc.* **11**, 1345–1359 (2016).
- Igamberdiev, A. U. & Gardeström, P. Regulation of NAD- and NADP-dependent isocitrate dehydrogenases by reduction levels of pyridine

- nucleotides in mitochondria and cytosol of pea leaves. *Biochim. Biophys. Acta* **117**–125, 1606 (2003).
34. Igamberdiev, A. U., Bykova, N. V., Lea, P. J. & Gardestrom, P. The role of photorespiration in redox and energy balance of photosynthetic plant cells: a study with a barley mutant deficient in glycine decarboxylase. *Physiol. Plant.* **111**, 427–438 (2001).
  35. Foyer, C. H. & Noctor, G. Ascorbate and glutathione: the heart of the redox hub. *Plant Physiol.* **155**, 2–18 (2011).
  36. Bassham, J. A., Shibata, K., Steenberg, K., Bourdon, J. & Calvin, M. The Photosynthetic cycle and respiration: light-dark transients. *J. Am. Chem. Soc.* **78**, 4120–4124 (1956).
  37. Berkemeyer, M., Scheibe, R. & Ocheretina, O. A novel, non-redox-regulated NAD-dependent malate dehydrogenase from chloroplasts of *Arabidopsis thaliana* L. *J. Biol. Chem.* **273**, 27927–27933 (1998).
  38. Engel, N. et al. Deletion of glycine decarboxylase in *Arabidopsis* is lethal under nonphotorespiratory conditions. *Plant Physiol.* **144**, 1328–1335 (2007).
  39. Gardestrom, P., Bergman, A. & Ericson, I. Inhibition of the conversion of glycine to serine in spinach leaf mitochondria. *Physiol. Plant.* **53**, 439–444 (1981).
  40. Ikezawa, N., Ifuku, K., Endo, T. & Sato, F. Inhibition of photosystem II of spinach by the respiration inhibitors piericidin A and thenoyltrifluoroacetone. *Biosci. Biotechnol. Biochem.* **66**, 1925–1929 (2002).
  41. Zhao, Y. Z. & Yang, Y. Real-time and high-throughput analysis of mitochondrial metabolic states in living cells using genetically encoded NAD<sup>+</sup>/NADH sensors. *Free Radic. Biol. Med.* **100**, 43–52 (2016).
  42. Wigge, B., Kromer, S. & Gardestrom, P. The redox levels and subcellular-distribution of pyridine-nucleotides in illuminated barley leaf protoplasts studied by rapid fractionation. *Physiol. Plant.* **88**, 10–18 (1993).
  43. Hashida, S. & Kawai-Yamada, M. Inter-organelle NAD metabolism underpinning light responsive NADP dynamics in plants. *Front. Plant Sci.* **10**, 960 (2019).
  44. Hashida, S. et al. Ferredoxin/thioredoxin system plays an important role in the chloroplastic NADP status of *Arabidopsis*. *Plant J.* **95**, 947–960 (2018).
  45. Palmieri, F. et al. Molecular identification and functional characterization of *Arabidopsis thaliana* mitochondrial and chloroplastic NAD<sup>+</sup> carrier proteins. *J. Biol. Chem.* **284**, 31249–31259 (2009).
  46. Bernhardt, K., Wilkinson, S., Weber, A. P. M. & Linka, N. A peroxisomal carrier delivers NAD plus and contributes to optimal fatty acid degradation during storage oil mobilization. *Plant J.* **69**, 1–13 (2012).
  47. Marty, L. et al. *Arabidopsis* glutathione reductase 2 is indispensable in plastids, while mitochondrial glutathione is safeguarded by additional reduction and transport systems. *New Phytol.* **224**, 1569–1584 (2019).
  48. Vauclare, P., Diallo, N., Bourguignon, J., Macherel, D. & Douce, R. Regulation of the expression of the glycine decarboxylase complex during pea leaf development. *Plant Physiol.* **112**, 1523–1530 (1996).
  49. Ros, R., Munoz-Bertomeu, J. & Krueger, S. Serine in plants: biosynthesis, metabolism, and functions. *Trends Plant Sci.* **19**, 564–569 (2014).
  50. Heineke, D. et al. Redox transfer across the inner chloroplast envelope membrane. *Plant Physiol.* **95**, 1131–1137 (1991).
  51. Tomaz, T. et al. Mitochondrial malate dehydrogenase lowers leaf respiration and alters photorespiration and plant growth in *Arabidopsis*. *Plant Physiol.* **154**, 1143–1157 (2010).
  52. Lindén, P., Keech, O., Stenlund, H., Gardeström, P. & Moritz, T. Reduced mitochondrial malate dehydrogenase activity has a strong effect on photorespiratory metabolism as revealed by <sup>13</sup>C labelling. *J. Exp. Bot.* **67**, 3123–3135 (2016).
  53. Winter, H., Robinson, D. G. & Heldt, H. W. Subcellular volumes and metabolite concentrations in spinach leaves. *Planta* **193**, 530–535 (1994).
  54. Bykova, N. V., Moller, I. M., Gardestrom, P. & Igamberdiev, A. U. The function of glycine decarboxylase complex is optimized to maintain high photorespiratory flux via buffering of its reaction products. *Mitochondrion* **19**, 357–364 (2014).
  55. Oliver, D. J. & Raman, R. Glycine decarboxylase - protein chemistry and molecular-biology of the major protein in leaf mitochondria. *J. Bioenerg. Biomembr.* **27**, 407–414 (1995).
  56. Oikawa, K. et al. Physical interaction between peroxisomes and chloroplasts elucidated by in situ laser analysis. *Nat. Plants* **1**, 15035 (2015).
  57. Sweetlove, L. J., Beard, K. F., Nunes-Nesi, A., Fernie, A. R. & Ratcliffe, R. G. Not just a circle: flux modes in the plant TCA cycle. *Trends Plant Sci.* **15**, 462–470 (2010).
  58. Lehmann, M. M. et al. Metabolic fate of the carboxyl groups of malate and pyruvate and their influence on delta C-13 of leaf-respired CO<sub>2</sub> during light enhanced dark respiration. *Front. Plant Sci.* **7**, 739 (2016).
  59. Schwarzlander, M. et al. Confocal imaging of glutathione redox potential in living plant cells. *J. Microsc.* **231**, 299–316 (2008).
  60. Hayashi, M., Aoki, M., Kondo, M. & Nishimura, M. Changes in targeting efficiencies of proteins to plant microbodies caused by amino acid substitutions in the carboxy-terminal tripeptide. *Plant Cell Physiol.* **38**, 759–768 (1997).
  61. Earley, K. W. et al. Gateway-compatible vectors for plant functional genomics and proteomics. *Plant J.* **45**, 616–629 (2006).
  62. Clough, S. J. & Bent, A. F. Floral dip: a simplified method for *Agrobacterium*-mediated transformation of *Arabidopsis thaliana*. *Plant J.* **16**, 735–743 (1998).
  63. De Col, V. et al. ATP sensing in living plant cells reveals tissue gradients and stress dynamics of energy physiology. *eLife* **6**, 26770 (2017).
  64. Murashige, T. & Skoog, F. A revised medium for rapid growth and bio assays with tobacco tissue cultures. *Physiol. Plant.* **15**, 473–497 (1962).
  65. Wagner, S. et al. Analysis of plant mitochondrial function using fluorescent protein sensors. *Methods Mol. Biol.* **1305**, 241–252 (2015).
  66. Fricker, M. D. Quantitative redox imaging software. *Antioxid. Redox Signal.* **24**, 752–762 (2016).
  67. Yoo, S. D., Cho, Y. H. & Sheen, J. *Arabidopsis* mesophyll protoplasts: a versatile cell system for transient gene expression analysis. *Nat. Protoc.* **2**, 1565–1572 (2007).
  68. Langhans R. W., Tibbitts T. *Plant Growth Chamber Handbook*. (Iowa State University, 1997).
  69. Usuda, H., Arron, G. P. & Edwards, G. E. Inhibition of glycine decarboxylation by aminoacetonitrile and its effect on photosynthesis in wheat. *J. Exp. Bot.* **31**, 1477–1483 (1980).
  70. Gardeström, P. Adenylate ratios in the cytosol, chloroplasts and mitochondria of barley leaf protoplasts during photosynthesis at different carbon-dioxide concentrations. *FEBS Lett.* **212**, 114–118 (1987).

## Acknowledgements

This project was supported by the National Natural Science Foundation of China (31870212), the Seed Funding Program for Basic Research (201811159131), the Hong Kong Research Grants Council Area of Excellence Scheme (AoE/M-403/16), and the Innovation and Technology Fund (Funding Support to State Key Laboratory of Agrobiotechnology) of the HKSAR, China. Any opinions, findings, conclusions, or recommendations expressed in this publication do not reflect the views of the Government of the Hong Kong Special Administrative Region or the Innovation and Technology Commission.”

## Author contributions

B.L.L. and S.L.L. designed the study. C.P.V. generated and characterized the ATP and pH sensor lines. X.G. generated the iNAP sensor constructs. S.L.L. produced the transgenic iNAP and SoNar sensor lines and carried out all the experiments. Y.Y. contributed to data analysis. B.L.L., S.L.L., and P.G. wrote the manuscript. All authors revised and approved the manuscript.

## Competing interests

The authors declare no competing interests.

## Additional information

Supplementary information is available for this paper at <https://doi.org/10.1038/s41467-020-17056-0>.

Correspondence and requests for materials should be addressed to B.L.L.

Peer review information *Nature Communications* thanks the anonymous reviewers for their contribution to the peer review of this work.

Reprints and permission information is available at <http://www.nature.com/reprints>

Publisher's note Springer Nature remains neutral with regard to jurisdictional claims in published maps and institutional affiliations.



**Open Access** This article is licensed under a Creative Commons Attribution 4.0 International License, which permits use, sharing, adaptation, distribution and reproduction in any medium or format, as long as you give appropriate credit to the original author(s) and the source, provide a link to the Creative Commons license, and indicate if changes were made. The images or other third party material in this article are included in the article's Creative Commons license, unless indicated otherwise in a credit line to the material. If material is not included in the article's Creative Commons license and your intended use is not permitted by statutory regulation or exceeds the permitted use, you will need to obtain permission directly from the copyright holder. To view a copy of this license, visit <http://creativecommons.org/licenses/by/4.0/>.

© The Author(s) 2020